9.21 Micro-PIV II

Contributed by:
S.T. Wereley and C.D. Meinhart

9.21.1 Flow in a Microchannel

No flow is more fundamental than the pressure driven flow in a straight channel of constant cross section. Since analytical solutions are known for most such flows, they prove invaluable for gauging the accuracy of μPIV.

Analytical Solution to Channel Flow

Although the solution to flow through a round capillary is the well-known parabolic profile, the analytical solution to flow through a capillary of a rectangular cross section is less well known. Since one of the goals of this section is to illustrate the accuracy of μPIV by comparing to a known solution, it is useful here to briefly discuss the analytical solution. The velocity field of flow through a rectangular duct can be calculated by solving the Stokes equation (the low Reynolds number version of the Navier-Stokes equation), with no-slip velocity boundary conditions at the wall [6] using a Fourier Series

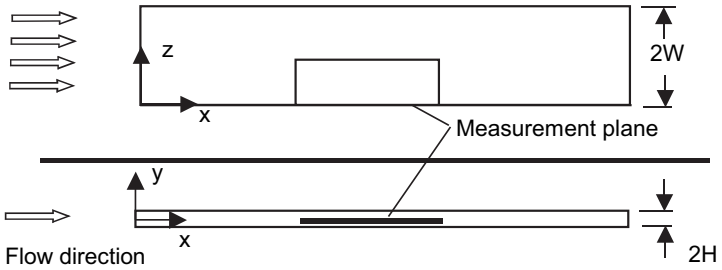

Fig. 9.97. Geometry of the microchannel. The microchannel is $2H$ high and $2W$ wide, and is assumed infinitely long in the axial direction. The measurement plane of interest is orientated in the $x - z$ plane and includes the microchannel wall at $z = 0$. The centerline of the channel is at $y = 0$. The microscope objective images the test section from below, in the lower part of the figure.

approach. Figure 9.97 shows a rectangular channel in which the width W is much greater than the height H. Sufficiently far from the wall (i.e., $Z \gg H$) the analytical solution in the Y direction (for constant Z), converges to the well-known parabolic profile for flow between infinite parallel plates. In the Z direction (for constant Y), however, the flow profile is unusual in that it has a very steep velocity gradient near the wall ($Z < H$) which reaches a constant value away from the wall ($Z \gg H$).

Experimental Measurements

A $30 \times 300 \times 25\,\mu\text{m}^3$ glass rectangular microchannel, fabricated by Wilmad Industries, was mounted flush to a $170\,\mu$m thick glass coverslip and a microscope slide. By carefully rotating the glass coverslip and the CCD camera, the channel was oriented to the optical plane of the microscope within $0.2°$ in all three angles. The orientation was confirmed optically by focusing the CCD camera on the microchannel walls. The microchannel was horizontally positioned using a high-precision $x - y$ stage, and verified optically to within $\sim 400\,$nm using epi-fluorescent imaging and image enhancement. The experimental arrangement is sketched in figure 9.97.

The flow in the glass microchannel was imaged through an inverted epi-fluorescent microscope and a Nikon Plan Apochromat oil-immersion objective lens with a magnification $M = 60$ and a numerical aperture NA = 1.4. The object plane was placed at approximately $7.5 \pm 1\,$mm from the bottom of the $30\,\mu$m thick microchannel . The Plan Apochromat lens was chosen for the experiment because it is a high quality microscope objective designed with low curvature of field, low distortion, and is corrected for spherical and chromatic aberrations.

Since deionized water (refractive index $n_\text{w} = 1.33$) was used as the working fluid but the lens immersion fluid was oil (refractive index $n_\text{i} = 1.515$), the

effective numerical aperture of the objective lens was limited to NA $\approx n_w/n_i = 1.23$ [14].

A filtered continuous white light source was used to align the test section with the CCD camera and to test for proper particle concentration. During the experiment, the continuous light source was replaced by the pulsed Nd:YAG laser. A Harvard Apparatus syringe pump was used to produce a 200 ml/h flow through the microchannel .

The particle-image fields were analyzed using a custom-written PIV interrogation program developed specifically for microfluidic applications. The program uses an ensemble-averaging correlation technique to estimate velocity vectors at a single measurement point by (1) cross-correlating particle-image fields from 20 instantaneous realizations, (2) ensemble averaging the cross-correlation functions, and (3) determining the peak of the ensemble-averaged correlation function. The signal-to-noise ratio is significantly increased by ensemble averaging the correlation function before peak detection, as opposed to either ensemble averaging the velocity vectors after peak detection, or ensemble averaging the particle-image field before correlation. The ensemble-averaging correlation technique is strictly limited to steady, quasi-steady, or periodic flows, which is certainly the situation in these experiments. This process is described in detail in section 5.4.2. For the current experiment, 20 realizations were chosen because that was more than a sufficient number of realizations to give an excellent signal, even with a first interrogation window of only 120×8 pixels.

The signal-to-noise ratio resulting from the ensemble-average correlation technique was high enough that there were no erroneous velocity measurements. Consequently, no vector validation postprocessing was performed on the data after interrogation. The velocity field was smoothed using a 3×3 Gaussian kernel with a standard deviation of one grid spacing in both directions.

Figure 9.98(a) shows an ensemble-averaged velocity-vector field of the microchannel. The images were analyzed using a low spatial resolution away from the wall, where the velocity gradient is low, and using a high spatial resolution near the wall, where the wall-normal velocity gradient is largest. The interrogation spots were chosen to be longer in the streamwise direction than in the wall-normal direction. This allowed for a sufficient number of particle images to be captured in an interrogation spot, while providing the maximum possible spatial resolution in the wall-normal direction. The spatial resolution, defined by the size of the first interrogation window, was 120×40 pixels in the region far from the wall, and 120×8 pixels near the wall. This corresponds to a spatial resolution of $13.6\,\mu\text{m} \times 4.4\,\mu\text{m}$ and $13.6\,\mu\text{m} \times 0.9\,\mu\text{m}$, respectively. The interrogation spots were overlapped by 50% to extract the maximum possible amount of information for the chosen interrogation region size according to the Nyquist sampling criterion. Consequently, the velocity vector spacing in the wall-normal direction was 450 nm near the wall. The streamwise velocity profile was estimated by line-averaging the measured ve-

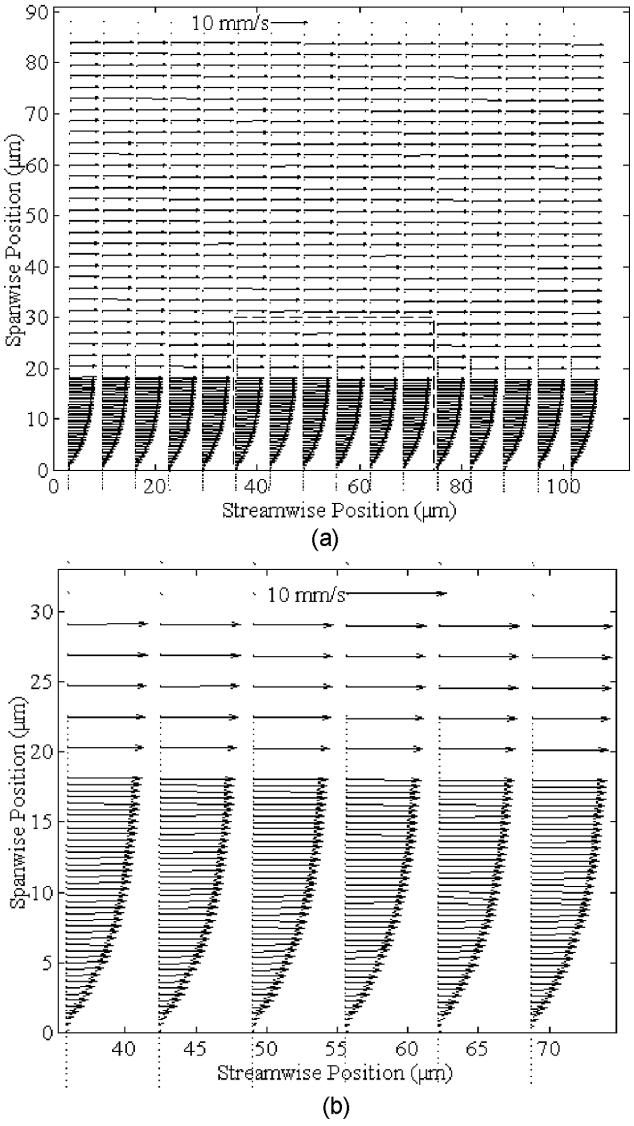

Fig. 9.98. (a) Large area view of ensemble-averaged velocity-vector field measured in a $30 \times 300 \times 25\,\mu\text{m}^3$ channel. The spatial resolution, defined by the interrogation spot size of the first interrogation window, is $13.6\,\mu\text{m} \times 4.4\,\mu\text{m}$ away from the wall, and $13.6\,\mu\text{m} \times 0.9\,\mu\text{m}$ near the wall [406]. (b) Near wall view of boxed region from (a).

locity data in the streamwise direction. Figure 9.99 compares the streamwise velocity profile estimated from the PIV measurements (shown as symbols) to the analytical solution for laminar flow of a Newtonian fluid in a rectangular channel (shown as a solid curve). The agreement is within 2% of full-scale resolution. Hence, the accuracy of μPIV is at worst 2% of full-scale for these experimental conditions. The bulk flow rate of the analytical curve was determined by matching the free-stream velocity data away from the wall. The wall

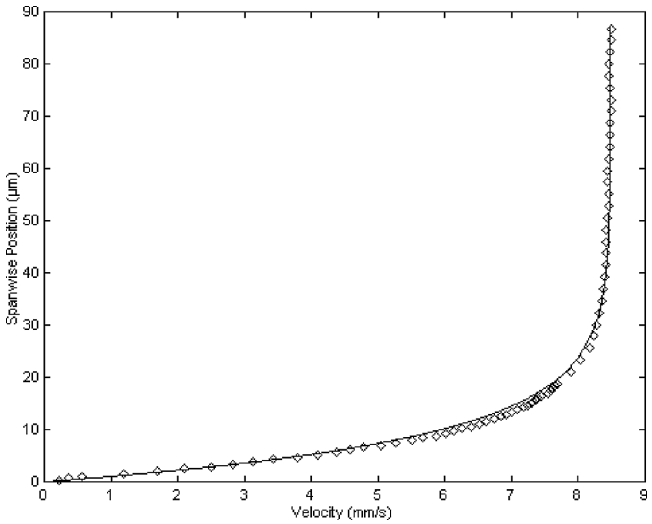

Fig. 9.99. Velocity profile measured in a nominally $30\,\mu\text{m} \times 300\,\mu\text{m}$ channel. The symbols represent the experimental PIV data while the solid curve represents the analytical solution [406].

position of the analytical curve was determined by extrapolating the velocity profile to zero near the wall.

Since the microchannel flow was fully developed, the wall-normal component of the velocity vectors is expected to be close to zero. The average angle of inclination of the velocity field was found to be small, 0.0046 rad, suggesting that the test section was slightly rotated in the plane of the CCD array relative to a row of pixels on the array. This rotation was corrected mathematically by rotating the coordinate system of the velocity field by 0.0046 rad. The position of the wall can be determined to within about 400 nm by direct observation of the image because of diffraction as well as the blurring of the out-of-focus parts of the wall. The precise location of the wall was more accurately determined by applying the no-slip boundary condition, which is expected to hold at these length scales for the combination of water flowing through glass, and extrapolating the velocity profile to zero at 16 different streamwise positions (figure 9.98a). The location of the wall at every streamwise position agreed to within 8 nm of each other, suggesting that the wall is extremely flat, the optical system has little distortion, and the PIV measurements are very accurate.

Most PIV experiments have difficulty measuring velocity vectors very close to the wall. In many situations, hydrodynamic interactions between the particles and the wall prevent the particles from traveling close to the wall, or background reflections from the wall overshadow particle images. By using 200 nm diameter particles and epi-fluorescence to remove background reflections, we have been able to make accurate velocity measurements to within about 450 nm of the wall; see figure 9.98.

9.21.2 Flow in a Micronozzle

The utility of these new imaging and processing algorithms along with the μPIV technique itself can be demonstrated by measuring the flow through a micronozzle. The micronozzles were designed to be operated with supersonic gas flows. In the initial stages of this investigation, however, they were operated with a liquid in order to assess the spatial resolution capabilities of the μPIV technique without having to push the temporal envelope simultaneously. Consequently, the converging-diverging geometry of the micronozzle served as a very small venturi. The micronozzles were fabricated by Bayt & Breuer (now at Brown University) at MIT in 1998. The two-dimensional nozzle contours were etched using DRIE in 300 μm thick silicon wafers. The nozzles used in these experiments were etched 50 μm deep into the silicon wafer. A single 500 μm thick glass wafer was anodically bonded to the top of the wafer to provide an end wall. The wafers were mounted to a macroscopic aluminum manifold, pressure sealed using O-rings and vacuum grease, and connected with plastic tubing to a Harvard Apparatus syringe pump.

The liquid (de-ionized water) flow was seeded with relatively large 700 nm diameter fluorescently-labeled polystyrene particles (available from Duke Scientific). The particles were imaged using an air-immersion $NA = 0.6$, $40\times$ objective lens, and the epi-fluorescent imaging system described in Chapter 8. A flow rate of 4 ml/h was delivered to the nozzle by the syringe pump.

Figure 9.100 is the velocity field inside a nozzle with a 15° half angle and a 28 μm throat. The velocity field was calculated using the CDI technique with image overlapping (10 image pairs) and image correction, as explained above. The interrogation windows measured 64×32 pixel in the x and y directions, respectively. When projecting into the fluid, the correlation windows were 10.9 μm $\times$ 5.4 μm in the x and y directions, respectively. The interrogation spots were overlapped by 50% in accordance with the Nyquist criterion, yielding a velocity-vector spacing of 5.4 μm in the streamwise direction and

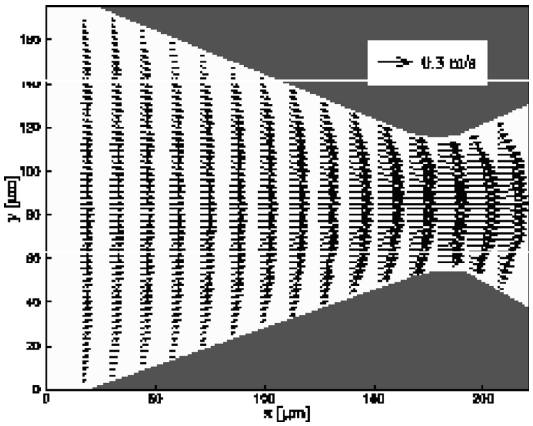

Fig. 9.100. Velocity field produced from 10 overlapped image pairs. The spatial resolution is 10.9 μm in the horizontal direction and 5.4 μm in the vertical direction. For clarity only every fifth column of measurements is shown [299]. Copyright 2002, AIAA. Reprinted with permission.

2.7 μm in the spanwise direction. The Reynolds number, based upon bulk velocity and throat width, is $Re = 22$.

Turning now from a converging geometry to a diverging geometry, we can explore whether instabilities well predicted by the Reynolds number at macroscopic length scales are indeed as well predicted by the Reynolds number at small length scales. The diffuser has a throat width of 28 μm and a thickness of 50 μm. The divergence half angle is quite large, 40°. The expected behavior for this geometry would be that at low Reynolds number s the flow would be entirely Stokes flow (i.e., no separation), but at larger Reynolds numbers, where inertial effects become important, separation should appear. Indeed, this is just what happens. At a Reynolds number of 22, the flow in the diverging section of the nozzle remains attached to the wall (not shown), while at a Reynolds number of 83, the flow separates as shown in figure 9.101. This figure is based on a single pair of images and as such represents an instantaneous snapshot of the flow. The interrogation region size measured $32 \times 32\,\text{pixel}^2$ or $5.4 \times 5.4\,\mu\text{m}^2$. A close inspection of figure 9.101 reveals that the separation creates a stable, steady vortex standing at the point of separation. After the flow has dissipated some of its energy in the vortex, it no longer has sufficient momentum to exist as a jet and it reattaches to the wall immediately downstream of the vortex. This is arguably the smallest vortex ever measured. Considering that the Kolmogorov length scale is frequently on the order of $0.1-1.0$ mm, μPIV has more than enough spatial resolution to measure turbulent flows at, and even significantly below, the Kolmogorov length scale. The example shown has 25 vectors measured across the 60 μm extent of the vortex.

9.21.3 Flow Around a Blood Cell

A surface tension driven Hele-Shaw flow with a Reynolds number of $3 \cdot 10^{-4}$ was developed by placing deionized water seeded with 300 nm diameter polystyrene particles between a 500 μm thick microscope slide and a 170 μm

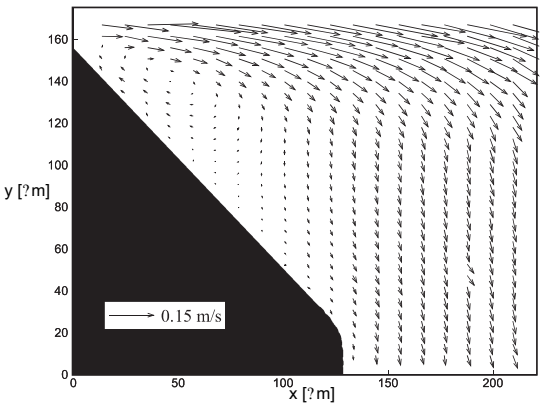

Fig. 9.101. Recirculation regions in a microdiffuser with spatial resolution of $5.4 \times 5.4\,\text{mm}^2$: (a) only every fourth column and every second row are shown for clarity; and (b) close up view of vortex region with all rows and columns of data shown [299]. Copyright 2002, AIAA. Reprinted with permission.

coverslip. Human red blood cells, obtained by autophlebotomy, were smeared onto a glass slide. The height of the liquid layer between the microscope slide and the coverslip was measured as approximately 4 μm by translating the microscope objective to focus on the glass surfaces immediately above and below the liquid layer. The translation stage of the microscope was adjusted until a single red blood cell was visible (using white light) in the center of the field of view. This type of flow was chosen because of its excellent optical access, ease of setup, and its 4 μm thickness, which minimized the contribution of out-of-focus seed particles to the background noise. Also, since red blood cells have a maximal tolerable shear stress, above which hemolysis occurs, this flow is potentially interesting to the biomedical community.

The images were recorded in a serial manner by opening the shutter of the camera for 2 ms to image the flow and then waiting 68.5 ms before acquiring the next image. Twenty-one images were collected in this manner. Since the camera is exposed to the particle reflections at the beginning of every video frame, each image can be correlated with the image following it. Consequently, the 21 images recorded can produce 20 pairs of images, each with the same time between exposures, Δt. Interrogation regions, sized 28×28 pixel, were spaced every 7 pixel in both the horizontal and vertical directions for a 75% overlap. Although technically, overlaps greater than 50% over sample the images, they effectively provide more velocity vectors to provide a better understanding of the velocity field.

Two velocity fields are shown in figure 9.102. Part (a) is the result of a forward difference interrogation (FDI) and part (b) is the result of a central difference interrogation (CDI). The differences between these two figures will be discussed below while the commonalities will be considered now. The flow exhibits the features that we expect from a Hele-Shaw flow. Because of the disparate length scales in a Hele-Shaw flow, with the thickness much smaller than the characteristic length and width of the flow, an ideal Hele-Shaw flow will closely resemble a two-dimensional potential flow [1]. However, because a typical red blood cell is about 2 μm, while the total height of the liquid layer between the slides is 4 μm, there is a possibility that some of the flow will go over the top of the cell instead of around it in a Hele-Shaw configuration. Since the velocity field in figure 9.102 closely resembles that of a potential flow around a right circular cylinder, we can conclude that the flow is primarily a Hele-Shaw flow. Far from the cylinder, the velocity field is uniformly directed upward and to the right at about a 75° angle from the horizontal. On either side of the red blood cell, there are stagnation points where the velocity goes to zero. The velocity field is symmetric with respect to reflection in a plane normal to the page and passing through the stagnation points. The velocity field differs from potential flow in that near the red blood cell there is evidence of the no-slip velocity condition. These observations agree well with the theory of Hele-Shaw.

For both algorithms, measurement regions that resulted in more than 20% of the combined area of the first and second interrogation windows inside of the

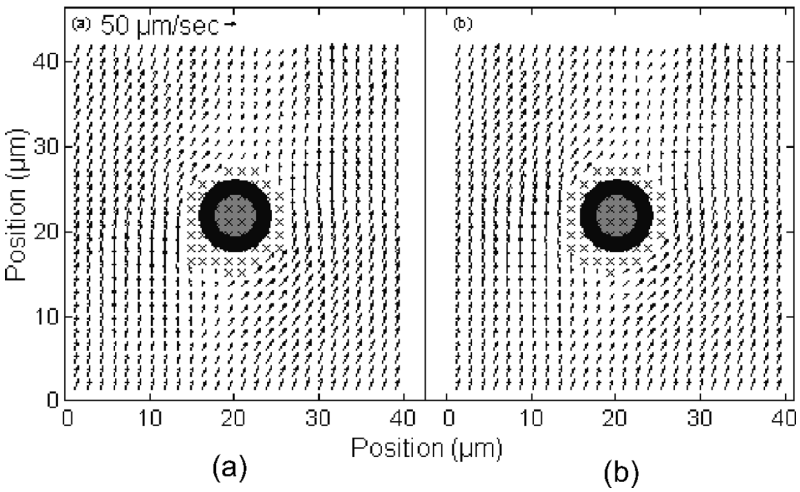

Fig. 9.102. Flow around a single human red blood cell: (a) forward difference adaptive window offset analysis; and (b) central difference adaptive window offset analysis. Cross symbols (×) indicate points that cannot be interrogated because they are too close to the cell [169].

blood cell are eliminated and replaced with a '×' symbol because they will tend to produce velocity measurements with serious errors. The central difference interrogation (CDI) scheme is able to accurately measure velocities closer to the surface of the cell than the forward difference interrogation (FDI) scheme. The CDI scheme has a total of 55 invalid measurement points, equivalent to $59.4\,\mu\text{m}^2$ of image area that cannot be interrogated, while the FDI has 57 invalid measurement points or $61.6\,\mu\text{m}^2$. Although this difference of two measurement points may not seem significant, it amounts to the area that the FDI algorithm cannot interrogate being 3.7% larger than the area the CDI algorithm cannot interrogate. Furthermore, the distribution of the invalid points is significant. By carefully comparing figure 9.102a with figure 9.102b, it is apparent that the FDI has three more invalid measurement points upstream of the blood cell than does the CDI scheme while the CDI scheme has one more invalid point downstream of the blood cell. This difference in distribution of invalid points translates into the centroid of the invalid area being nearly twice as far from the center of the blood cell in the FDI case ($0.66\,\mu$m, or 7.85%, of the cell diameter) versus the CDI case ($0.34\,\mu$m, or 4.05%, of the cell diameter). This difference means that the FDI measurements are less symmetrically distributed around the blood cell than the CDI measurements are. In fact, they are biased toward the time the first image was recorded. Computing the average distance between the invalid measurement points and the surface of the blood cell indicates how closely to the blood cell surface each algorithm will allow the images to be accurately interrogated. On average, the invalid measurement points bordering the red blood cell generated using the

FDI scheme are 12% farther from the cell than the invalid measurement points generated with the CDI scheme. Consequently, the adaptive CDI algorithm is more symmetric than the adaptive FDI algorithm and also allows measuring the velocity field nearer the cell surface.

9.21.4 Flow in Microfluidic Biochip

Microfluidic biochips are microfabricated devices that are used for delivery, processing, and analysis of biological species (molecules and cells). Gomez et al. [400] successfully used μPIV to measure the flow in a microfluidic biochip designed for impedance spectroscopy of biological species. This device was studied further in [415]. The biochip is fabricated in a silicon wafer with a thickness of 450 μm. It has a series of rectangular test cavities ranging from tens to hundreds of microns on a side, connected by narrow channels measuring 10 μm across. The whole pattern is defined by a single anisotropic etch of single crystal silicon to a depth of 12 μm. Each of the test cavities has a pair or series of electrodes patterned on its bottom. The array of test cavities is sealed with a piece of glass of about 0.2 mm thick, allowing optical access to the flow. During the experiment, water-based suspensions of fluorescein-labeled latex beads with a mean diameter of 1.88 μm were injected into the biochip and the flow was illuminated with a constant intensity mercury lamp. Images are captured with a CCD camera through an epi-fluorescence microscope and recorded at a video rate (30 Hz). One of the PIV images covering an area of $542 \times 406\,\mu\text{m}^2$ on the chip with a digital resolution of 360×270 pixel is shown in figure 9.103. The flow in a rectangular cavity of the biochip is determined by evaluating more than 100 μPIV recording pairs with the ensemble correlation method, CDI, and the image correction technique, and the results are given in figure 9.104. An interrogation window of 88 pixel is chosen

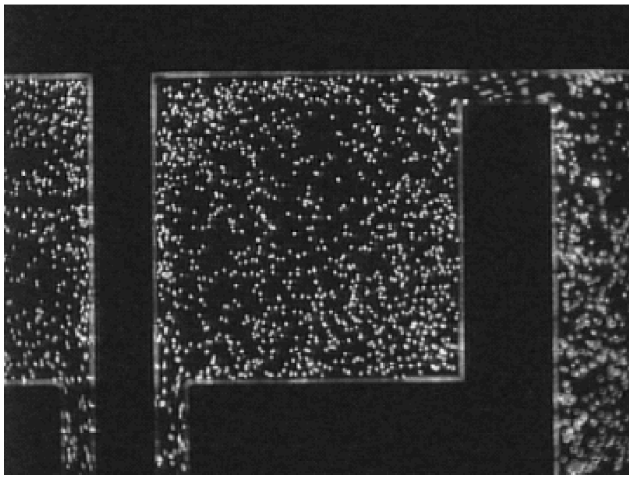

Fig. 9.103. Digital image of the seeded flow in the cavities and channels of the biochip (360×270 pixel, $542 \times 406\,\mu\text{m}^2$) [415]. Copyright 2001, AIAA. Reprinted with permission.

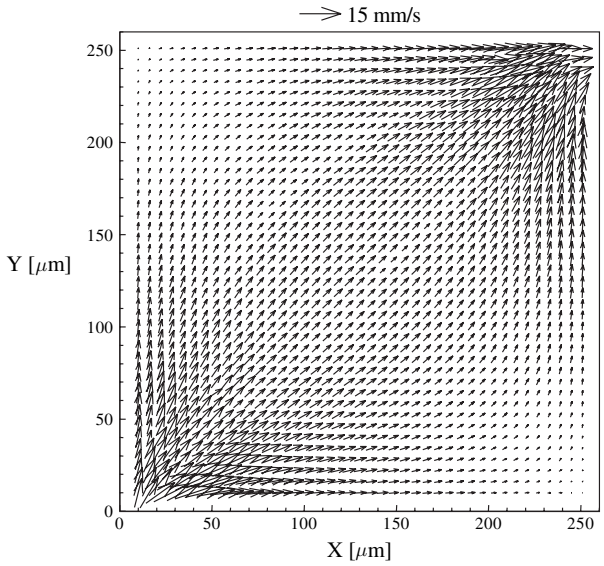

Fig. 9.104. PIV measurement results in a rectangular cavity of the biochip with a spatial resolution of $12 \times 12\,\mu\text{m}^2$ [299]. Copyright 2001, AIAA. Reprinted with permission.

for the PIV image evaluation, so that the corresponding spatial resolution is about $12 \times 12\,\mu\text{m}^2$. The measured velocities in the cavity range from about 100 mm/s to 1600 μm/s.

This biochip can function in several different modes, one of which is by immobilizing on the electrodes antibodies specific to an antigen being sought. The rate at which the antibodies capture the antigens will be a function of the concentration of the antigens in the solution as well as the solution flux past the electrodes. Consequently, knowledge of the velocity field is critical to characterizing the performance of the biochip. Since this is an example of the μPIV technique, the reader is directed to [400] for more details about the biochip performance characterization.